Amplification of Superconducting Fluctuations in Driven YBa$_2$Cu$_3$O$_{6+x}$

A. von Hoegen,[1] M. Fechner,[1] M. Först,[1] N. Taherian,[1] E. Rowe,[1] A. Ribak,[1] J. Porras,[2]
B. Keimer,[2] M. Michael,[3] E. Demler,[3] and A. Cavalleri[1,4,*]

[1]*Max Planck Institute for the Structure and Dynamics of Matter, 22761 Hamburg, Germany*
[2]*Max Planck Institute for Solid State Research, 70569 Stuttgart, Germany*
[3]*Department of Physics, Harvard University, Cambridge, Massachusetts 02138, USA*
[4]*Department of Physics, University of Oxford, Oxford OX1 3PU, United Kingdom*

In cuprate high-T_c superconductors, resonant excitation of certain lattice vibrations has been shown to induce transient terahertz reflectivity features suggestive of nonequilibrium superconductivity above the critical temperature T_c. A microscopic mechanism for these observations is still lacking. Here, time-resolved measurements of scattering-angle- and polarization-dependent second-harmonic generation in driven YBa$_2$Cu$_3$O$_{6+x}$ reveal a three-order-of-magnitude amplification of a 2.5-THz electronic mode, which is unique because of its symmetry, momentum, and temperature dependence. A theory for amplification of finite-momentum Josephson plasma polaritons, which are assumed to be well formed below T_c but incoherent throughout the pseudogap phase, explains all these observations. A theoretical solution for the Fresnel-Floquet reflection that starts from the coherently oscillating Josephson plasma polaritons provides a possible mechanism for the nonequilibrium superconductorlike terahertz reflectivity reported earlier. Beyond the immediate case of cuprates, this work underscores the role of nonlinear mode mixing to amplify fluctuating modes above the transition temperature in a wide range of materials.

The possibility of enhancing desirable functional properties using mode-selective electromagnetic drives has motivated a series of studies of the nonlinear terahertz-frequency properties in quantum materials [1–12]]. In particular, the nonlinear excitation of apical oxygen vibrations in underdoped YBa$_2$Cu$_3$O$_{6+x}$ has been shown to induce transient optical signatures of superconductivity up to the pseudogap temperature T^*, as evidenced by characteristic edges in time-resolved terahertz reflectivity measurements [13–16]. A comprehensive understanding of this phenomenon is still lacking, although femtosecond soft and hard x-ray scattering measurements have underscored the role of nonlinearly driven lattice vibrations, the melting of competing charge orders [17], and the transient deformation of the crystal structure [18,19]. Experimentally, characterization of the effect of these nonlinearly driven lattice

vibrations calls for new methods, which should expose the response of all modes of the system at a variety of momenta. In particular, experiments that characterize the dynamics of both symmetry even and symmetry odd modes is required.

Here, femtosecond midinfrared pulses with polarization aligned along the c axis of YBa$_2$Cu$_3$O$_{6.48}$ and YBa$_2$Cu$_3$O$_{6.65}$ [see Fig. 1(a)] were used to resonantly drive the same 17- and 20-THz apical oxygen oscillations that induce the superconductorlike terahertz reflectivity discussed above. Unlike all previous measurements, the carrier-envelope-phase (CEP) offset of the pump pulses was stabilized [20,21], enabling subcycle sampling of the coherent dynamics of the driven phonons, and of nonlinearly coupled excitations, in a repetitive pump-probe experiment. Near-infrared probe pulses of 30-fs duration and linear polarization aligned with the same c-axis direction of the midinfrared excitation were used to simultaneously record the time-dependent linear reflectivity $\Delta R(t)$ at 800-nm wavelength [Fig. 1(b)] and the time-dependent 400-nm second-harmonic (SH) intensity $\Delta I_{SH}(t)$ [Fig. 1(c)] [22]. The induced $\Delta R(t)$ and $\Delta I_{SH}(t)$ were characterized by a prompt change as pump and probe pulses overlapped in time, followed by a smooth decay with superimposed coherent oscillations.
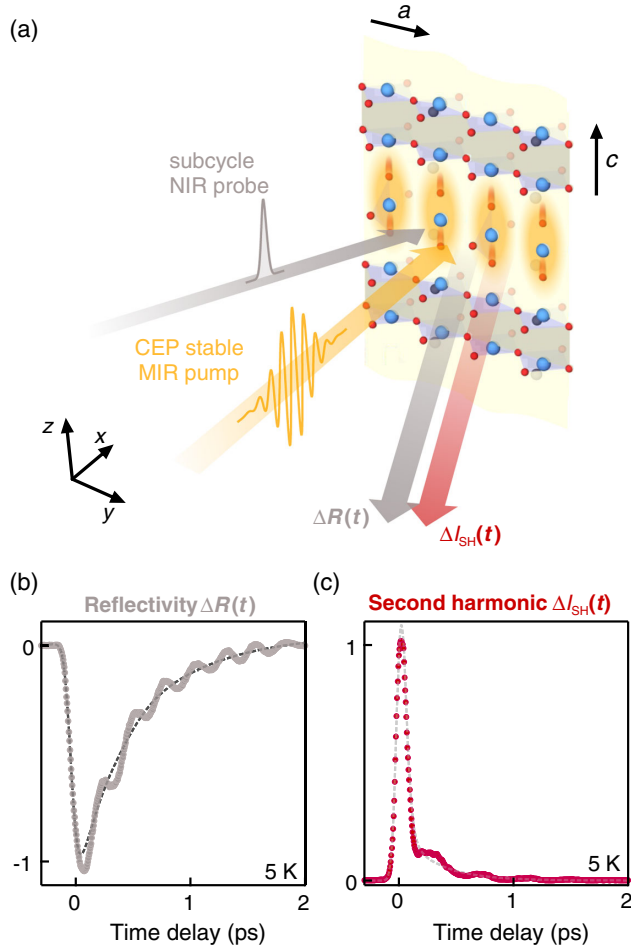
FIG. 1. (a) Schematic of the pump-probe geometry. The 800-nm near-IR probe (gray) and CEP stable mid-IR (MIR) pump (yellow) pulses were polarized along the $YBa_2Cu_3O_{6.48}$ crystal's *c*-axis and perpendicular to the CuO_2 planes. The resonantly excited apical oxygen vibrations are shaded in yellow. Light at the fundamental (gray arrow) and second-harmonic (red arrow) frequency is reflected from the sample. (b) Time-resolved changes of the linear reflectivity at 800-nm wavelength, showing coherent modulations due to fully symmetric Raman phonon modes. (c) Time-resolved second-harmonic intensity at 400-nm wavelength (red circles) and a numerical fit to the nonoscillatory component of the signal (dashed line). The data in (b) and (c) are shown for 5-K base temperature and 7-MV/cm peak excitation field.

In a centrosymmetric medium, oscillations in $\Delta R(t)$ encode the coherent excitation of *symmetry-even* (Raman-active) modes at zero momentum ($q = 0$). Here, two totally symmetric A_g modes at 3.7 and 5 THz are most clearly observed, triggered by third-order coupling to the driven apical oxygen phonon [1]. Similar measurements have already been discussed in Ref. [23] for a different doping and are discussed in the Supplemental Material [24].

On the contrary, oscillations in the second-harmonic intensity $\Delta I_{SH}(t)$ are sensitive to coherent *symmetry-odd* (infrared-active) modes [25,26], and provide important clues for the microscopic dynamics in this material. The

underlying detection process is intuitively understood by noting that in a medium, in which $\chi^2(\omega_{IR}, \omega_{IR}) \sim 0$ at equilibrium, a coherent symmetry-odd mode breaks inversion symmetry twice a cycle as it oscillates at ω_{mode}. Here, ω_{IR} denotes the frequency of the infrared probe field $E(\omega_{IR})$ and ω_{mode} is the frequency of the oscillating symmetry-odd mode.

More precisely, $\Delta I_{SH}(t)$ is generated by a *four-wave* process that mixes the field $E(\omega_{mode})$ of the coherently oscillating symmetry-odd mode with the infrared probe field $E(\omega_{IR})$. A third-order nonlinear polarization $P^{(3)}(\omega) = \chi^3(\omega_{IR}, \omega_{IR}, \omega_{mode})E(\omega_{IR})E(\omega_{IR})E(\omega_{mode})$ is generated at $2\omega_{IR} \pm \omega_{mode}$. In the limit in which the probe pulse duration is much shorter than the mode period $T_{mode} = 2\pi/\omega_{mode}$, as is the case here, for a fixed pump-probe time delay t the third-order susceptibility $\chi^3(\omega_{IR}, \omega_{IR}, \omega_{mode})$ can be thought of as an effective second-order susceptibility $\chi^2_{eff,t}(\omega_{IR}, \omega_{IR})$, which evolves with the delay t and tracks the coherent mode oscillations in time. The second-order susceptibility in turn generates a time-delay-dependent effective second order polarization $P^{(2)}_{eff,t}(\omega) = \chi^2_{eff,t}(\omega_{IR}, \omega_{IR})E(\omega_{IR})E(\omega_{IR})$ which radiates a time-delay-dependent optical field $E^{(2)}_t(\omega)$ at the second harmonic $2\omega_{IR}$ of the probe pulse. In the present geometry, we detect this optical field together with a second-harmonic reference field, generated before the sample, polarized along the same direction as the incoming probe beam at 800 nm and characterized independently (see Supplemental Material [24]). This measurement enables detection of a heterodyned time-delay-dependent oscillation at ω_{mode} in the second-harmonic intensity $\Delta I_{SH}(t)$. Crucially, such heterodyned detection provides a measure of all coherently excited symmetry-odd modes at their respective eigenfrequencies.

Note that the above is a different measurement from *time-integrated* second-harmonic generation experiments reported extensively in the past [27], which descend from a time-independent second-order susceptibility $\chi^2(\omega_{IR}, \omega_{IR})$.

In Fig. 2, we report representative time-resolved second-harmonic data taken in the superconducting state of $YBa_2Cu_3O_{6.48}$ at $T = 5$ K ($T_c = 48$ K). These experiments were conducted for a range of pump electric field strengths between 300 KV/cm [see Figs. 2(a) and 2(b)] to 7 MV/cm [see Figs. 2(e) and 2(f)]. The oscillatory part of the time-resolved second-harmonic intensity $\Delta I_{SH}(t)$ was extracted from the traces displayed in Fig. 1(c) by subtracting the slowly varying signal contributions. The data shown in Fig. 2(a) (shaded in yellow), and the corresponding Fourier transform in Fig. 2(b), are representative of resonant excitation of two modes at 17 and 20 THz, which were simultaneously driven by the broad spectrum of the ultrashort pump pulse.

The higher field data reported in Figs. 2(c) and 2(d) (500 KV/cm) and Figs. 2(e) and 2(f) (7 MV/cm) reflect a nonlinear response regime, where other nonlinearly
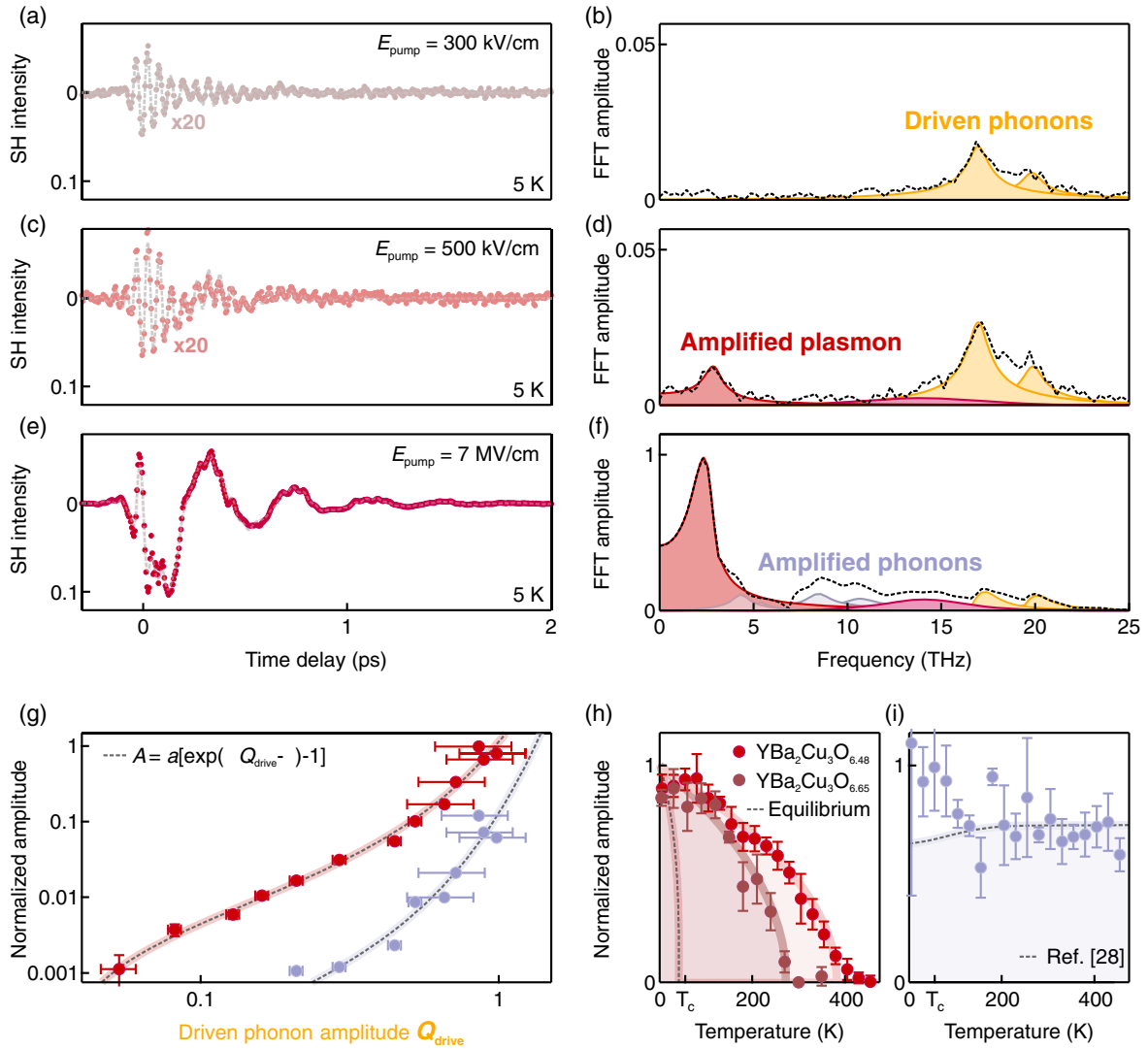
FIG. 2.   (a),(b) Coherent SH signal at the lowest excitation field ($E = 0.3$ MV/cm) and the corresponding Fourier amplitude spectrum at $T = 5$ K, well below the critical temperature $T_c = 48$ K. The high-frequency oscillations at 17 and 20 THz (yellow peaks) are coherent symmetry breaking apical oxygen vibrations, resonantly driven by the excitation pulse. (c),(d) Coherent SH response at higher excitations fields ($E = 0.5$ MV/cm) at the same temperature. The peaks at $\nu_1 = 2.5$ THz and $\nu_2 = 14.5$ THz (red and magenta) are ascribed to coherent oscillations of Josephson plasma waves. (e),(f) The coherent SH response at significantly stronger excitations ($E = 7$ MV/cm) show the same coherences of (c) and (b), with additional modes drawn as gray peaks. These additional peaks are dominated by those at 8.6 and 10.5 THz and label additional phonons nonlinearly coupled to the resonantly driven lattice modes. (g) Measured amplitude of the amplified low-frequency JPP J_1 and the amplified phonon amplitude $Q_{amplified}$ plotted as a function of the driven apical oxygen vibration amplitude Q_{drive}. All quantities were extracted from the same time trace, for different strengths of the midinfrared excitation field. The dashed line is an exponential fit $A(Q_{drive}) = a \cdot (e^{\alpha Q_{drive} - \beta} - 1)$ to the data, where the gain factor α is determined by the strength of the coupling between the driven phonon and the JPP and $\beta > 0$ is the amplification threshold. Error bars represent the standard deviation σ of the amplitudes extracted by numerical fits. (h) Full temperature dependence of the JPP peaks in (d) (shaded area) for $YBa_2Cu_3O_{6.48}$ (red) and $YBa_2Cu_3O_{6.65}$ (dark red). The lines are fits to the data with a mean-field approach $\propto \sqrt{1 - T/T'}$, yielding $T' = 380$ K for $YBa_2Cu_3O_{6.48}$ and $T = 280$ K for $YBa_2Cu_3O_{6.65}$. The dashed line is the temperature dependence of the equilibrium low-frequency Josephson plasma resonance in $YBa_2Cu_3O_{6.5}$, which disappears at T_c. (i) Temperature dependence of the amplitude of the nonlinearly coupled infrared active phonons at 8.5 and 10 THz. Their temperature dependence from equilibrium infrared measurements in $YBa_2Cu_3O_{6.5}$, taken from Ref. [28], is shown as a dashed line. The data in (h) and (i) were recorded at an excitation peak field of ~ 7 MV/cm. Error bars represent the standard deviation σ of the amplitudes obtained by repeating the experiment under equivalent conditions.

coupled modes responded to the resonant excitation of the directly driven vibrations. One nonlinearly coupled mode (shaded in red) stands out already at the low fields [Figs. 2(c) and 2(d)], oscillating at 2.5-THz frequency, for which no c-axis symmetry-odd vibration is expected [28–32]. The simultaneous measurements of the linear reflectivity $\Delta R(t)$ rule out that this oscillation results from a coherently excited Raman mode (see Supplemental Material [24]). The amplitude of this mode increased more than 100-fold as the pump electric field was increased from 0.5 to 7 MV/cm [Figs. 2(d) and 2(f)], evidencing a regime of amplification that will be analyzed in the remainder of the paper.

Other resonances were also observed in the SH spectrum recorded for the highest excitation fields [see Figs. 2(e) and 2(f)], including two infrared active phonons at 8.6 and 10.5 THz (shaded in gray) [28,32] and a broad feature centered around 14 THz, reminiscent of an intrabilayer Josephson plasma [29]. Experiments conducted for $YBa_2Cu_3O_{6.65}$ yielded similar results, with one amplified mode emerging at frequencies where no infrared-active phonons are expected, oscillating at 2.8 THz as opposed to 2.5 THz for this higher doping level (see Supplemental Material [24]).

The multicomponent oscillations reported in Figs. 2(a), 2(c), and 2(d) were filtered in frequency, and yielded the amplitude of each mode, e.g., $J_1 \propto \Delta I_{SH}(t)_{\omega=2.5 \text{ THz}}$ or $Q_{amplified} \propto \Delta I_{SH}(t)_{\omega=8.6 \text{ THz}}$ (see Supplemental Material [24]). The same could be done for $Q_{drive} \propto \Delta I_{SH}(t)_{\omega=17 \text{ THz}}$ and we could then extract the growth of the amplified modes as a function of the drive $J_1(Q_{drive})$ and $Q_{amplified}(Q_{drive})$, as displayed in Fig. 2(g). We found that above a characteristic threshold value for the drive amplitude, each nonlinearly coupled oscillation grew exponentially. The low-frequency mode J_1 was amplified by at least 3 orders of magnitude in amplitude when increasing Q_{drive} by a factor of 10 [see Fig. 2(g)]. Similar exponential growth was found for the high-frequency mode $J_2 \propto \Delta I_{SH}(t)_{\omega=14.5 \text{ THz}}$, as shown in the Supplemental Material [24].

In Figs. 2(h) and 2(i), we report the temperature dependence $J_1(T)$ at the two doping levels analyzed here and $Q_{amplified}(T)$. These data show that the 2.5-THz oscillations in $YBa_2Cu_3O_{6.48}$ and the 2.8-THz mode in $YBa_2Cu_3O_{6.65}$ do not follow the temperature dependence of any one of the equilibrium modes. Indeed, in equilibrium one finds a 1-THz frequency Josephson plasma resonance, which disappears at T_c [see dashed curve in Fig. 2(h)], and a number of phonon resonances, which remain large above T_c [see dashed curve in Fig. 2(i)]. On the other hand, the quantity $J_1(T)$ plotted in Fig. 2(h) decayed only at a characteristic temperature scale T'. An empirical fit function proportional to $\sqrt{1 - T/T'}$ yielded $T' \approx 380$ K and $T' \approx 280$ K for $YBa_2Cu_3O_{6.48}$ and for the $YBa_2Cu_3O_{6.65}$, respectively. These temperature scales agree well with

the corresponding pseudogap temperatures T^* for each doping [33]. Finally, this temperature dependence is different from that of the amplified infrared active phonons [see Fig. 2(i)], which except for an anomaly close to T_c follow the temperature dependence of the corresponding equilibrium phonon modes [28], remaining of constant amplitude for all temperatures (see Supplemental Material [24]).

The symmetry of the 2.5-THz mode was measured as sketched in Fig. 3(a), by repeating all the SH measurements of Fig. 2 as a function of polarization angle φ for the incoming 800-nm probe pulses, while the 400-nm second-harmonic intensity was measured with an analyzer along the c axis (s polarization). All the data reported in Fig. 3 were acquired at room temperature, for which the polarization dependence was very similar to those collected at $T < T_c$. Additional measurements with the analyzer aligned along the a axis (p polarization) are reported in the Supplemental Material [24]. These SH polarimetry measurements yielded two-dimensional maps as a function of polarization angle and pump-probe time delay, as shown in the representative plot of Fig. 3(b). With the knowledge of the different mode frequencies extracted from the experiments of Fig. 2, we frequency filtered these two-dimensional plots, and extracted time-resolved SH polarimetry measurements for each mode (see Supplemental Material for details [24]). In Figs. 3(c)–3(e), we compare the symmetry of the driven 17- and 20-THz phonons (yellow), of the amplified 8.6- and 10.5-THz phonons (gray), and of the 2.5-THz mode (red), displayed at one representative time delay ($t = 150$ fs).

As shown in Figs. 3(c) and 3(d), the directly driven phonons (yellow) and the amplified phonons (gray) reflect a $Pmm2$ space group, that is, one in which one mirror symmetry of the equilibrium $Pmmm$ space group is broken periodically during the oscillation. This is consistent with the behavior expected for the B_{1u}-symmetry oscillations of these phonons. In contrast with all driven and amplified phonons, the angular dependence of the 2.5-THz mode shown in Fig. 3(e), is unique, being indicative of a lower symmetry for which at least two mirrors of the equilibrium $YBa_2Cu_3O_{6+x}$ structure are lost (Pm or lower symmetry). In addition, and in stark contrast to the phonons, the angular-dependent response exhibits a number of nodes, with the electronic mode changing sign as a function of polarization angle φ.

We further investigated the nature of the room temperature 2.5-THz mode by measuring SH spectra as a function of outgoing scattering angle, a reporter of their in-plane momentum. The 400-nm second-harmonic emission is sensitive to momenta in excess of 10^4 cm^{-1}, which for the 2.5-THz excitation is far larger than the corresponding light cone momentum accessible by linear terahertz spectroscopy (~ 80 cm^{-1}). As sketched in Fig. 4(a), these momentum-resolved measurements were obtained by aligning the midinfrared pump and the 800-nm probe
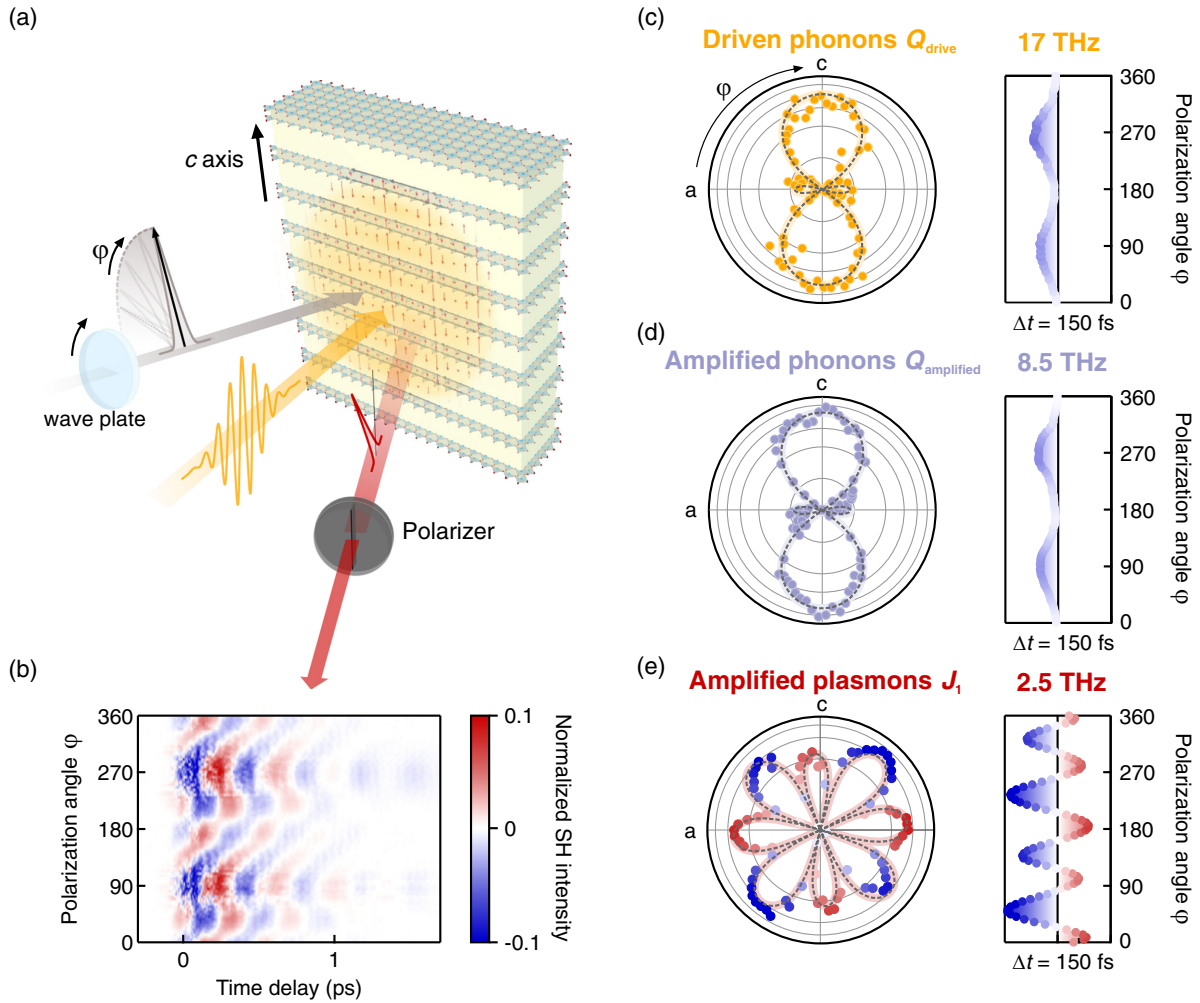
FIG. 3. (a) Schematic of the SH polarimetry geometry. The polarization angle φ of 800-nm near-infrared probe pulses (gray) is controlled by rotating a $\lambda/2$ waveplate. The reflected second-harmonic light (red arrow) passes through an analyzer to measure the different polarization components individually. (b) SH signal as a function of polarization angle and pump-probe time delay, measured at room temperature. (c)–(e) Normalized polarimetry signal of the driven phonons (yellow dots), amplified phonons (gray dots), and amplified JPPs (red and blue dots) for an analyzer oriented along the crystal's c axis, at one time delay $t = 150$ fs. The SH polarimetry signal of the two sets of phonons can be reproduced by a fit to a second-harmonic tensor with $mm2$ point group symmetry (dashed line) and the phase of the oscillations is polarization angle φ independent. The polarimetry signal of the amplified JPP agrees with a fit to a point group of lower symmetry (dashed line), in which at least two mirrors are lost. The phase of the coherent oscillations is periodically modulated with polarization angle φ, indicated by the red and blue color coding. The SH polarimetry data were recorded at room temperature with a peak field strength of ~5 MV/cm.

pulses collinearly with one another, and by measuring the SH signal for a series of outgoing scattering angles using a slit (see Supplemental Material [24]). The crucial observation is that while all directly driven (yellow) and amplified (gray) phonon signals peaked for specular reflection, corresponding to driven or amplified vibrations with zero in-plane momentum ($q_x = 0$), the 2.5-THz mode (red) peaked at finite in-plane momenta $q_x = \pm190$ cm^{-1}.

In the following, we present a possible theory that connects the observed amplified 2.5-THz (2.8-THz) modes to the nonlinear physics of Josephson plasma polaritons (JPP) [34], dispersive c-axis plasma waves made up of interlayer tunneling currents and propagating along the

CuO_2 planes [35]. In bilayer $YBa_2Cu_3O_{6+x}$, two JPP modes are found below T_c [36,37]. At zero momentum, these two modes are dominated by current flow between bilayers (lower-frequency mode) and within the bilayers (higher-frequency mode), depicted in Fig. 5(d). The zero-momentum frequencies for these modes are well known, although their momentum dependence has never been documented. As the momentum along the propagation direction changes, these JPP modes are no longer solely made up of c-axis currents, but involve also in-plane superflow, with a dispersion determined by the inductive response of the planes. In Figs. 5(a) and 5(b), we display their computed equilibrium dispersion curves, obtained
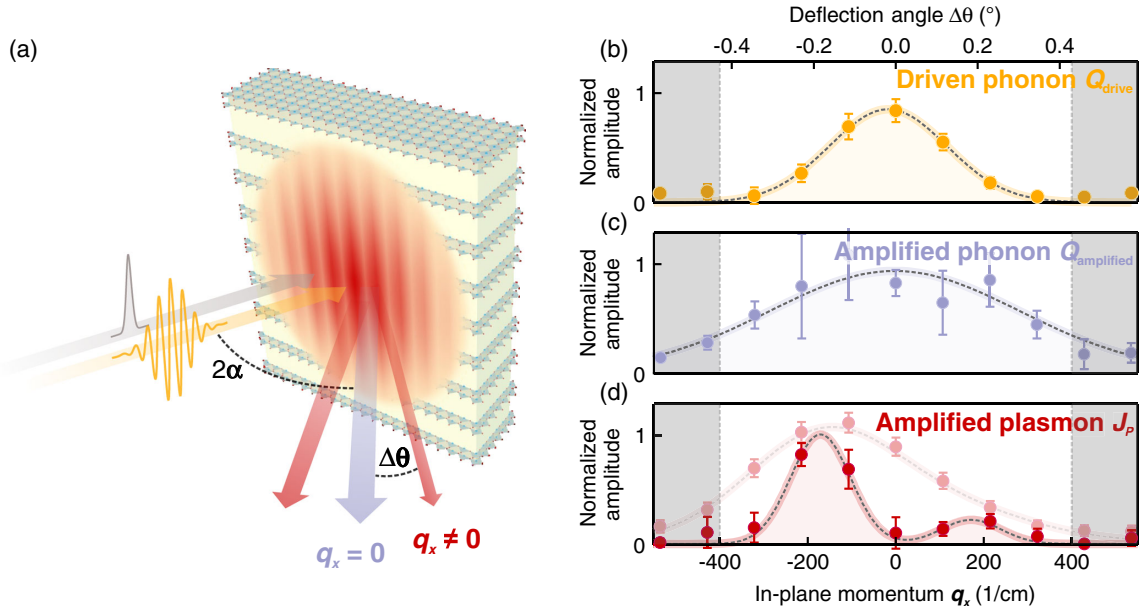
FIG. 4. (a) Schematic of the collinear geometry, where pump and probe beams are aligned collinear to excite the sample at an incidence angle α to the surface normal. The specular linear reflection at 800 nm (gray arrow) obeys Snell's law and leaves the sample with the same angle α. A finite-momentum transfer, due to scattering of propagating modes, appears as a deflection $\Delta\theta$ from the specular deflection (red arrows). (b)–(d) Momentum distribution of the driven phonons, amplified phonons, and amplified JPPs, measured at room temperature. Panel (d) shows the raw data (light red) together with deconvolved data (dark red), using the measured Gaussian profile of the $q = 0$ pump electric field induced SH response. The gray shaded areas denote the maximum accessible momentum of the experiment. For all the raw data in (b)–(d), error bars represent the standard deviation σ of the amplitudes extracted from numerical fits to the time-resolved second-harmonic intensity changes. The error bars of the deconvolved data (d) are determined from the deviation of the least squares fit, used in the deconvolution, to the raw data points (see Supplemental Material [24]). The data were recorded at room temperature with a peak field strength of $\sim$5 MV/cm.

from known zero-momentum frequencies and in-plane inductance (see Supplemental Material for details [24]).

To derive the nonlinear equations of motion for these JPP modes, and the coupling to the driven lattice vibrations, one first needs to supplement Maxwell equations with the relations between the supercurrents and electromagnetic fields [38]. The latter can be obtained directly from the kinetic energies of the interlayer tunneling and of the in-plane superflow, referred to here as $E_{J,\text{tunn}}$ and $E_{J,\text{plane}}$, respectively. The expression for these energies is $E_{J,\text{tunn}} = -J_{n,n+1}\cos[\theta_n - \theta_{n+1} - (2e/c)\int_{z_n}^{z_{n+1}} A_z dz]$ and $E_{J,\text{plane}} = \frac{1}{2}\rho_s v_s^2$. Here, $\theta_n(x,y,t)$ is the order parameter within each CuO_2 layer n, ρ_s denotes the local superfluid density, and $v_s = \nabla_{x,y}\theta_n - (2e/c)A$ is the in-plane superfluid velocity, which itself is a function of the in-plane order parameter gradient $\nabla_{x,y}\theta_n$ and of the vector potential A. In these expressions, $2e$ is the Cooper pair charge and c the speed of light.

The apical oxygen phonons excited by the pump to amplitude Q_{drive} are symmetry odd, and therefore modify the local superfluid densities in the $YBa_2Cu_3O_{6+x}$ bilayer structure in a way that is antisymmetric with respect to the two layers, $\delta\rho_{s\{1,2\}} \propto \pm Q_{\text{drive}}$ [38]. The effect of these vibrations on the in-plane superflow is then to increase and

decrease the in-plane kinetic energy $E_{J,\text{plane}}$ in neighboring planes in an oscillatory fashion, which can be written as $\delta E_{J,\text{plane}} = \delta\rho_{s1}v_{s1}^2 + \delta\rho_{s2}v_{s2}^2$ (see Supplemental Material for details [24]). This expression can be rewritten as $\delta E_{J,\text{plane}}(t) \propto Q_{\text{drive}}(t)(v_{s1} - v_{s2})(v_{s1} + v_{s2})$ or, equivalently, as $\delta E_{J,\text{plane}}(t) \propto Q_{\text{drive}}(t)J_1 J_2$, as the apical oxygen oscillations of coordinate Q_{drive} and the two finite-momentum tunneling modes are excited with $J_1 \propto v_{s1} - v_{s2}$ and $J_2 \propto v_{s1} + v_{s2}$, respectively. Intuitively, the c-axis currents J_1 and J_2 are driven by the lattice excitation because the changes in the in-plane kinetic energy also perturb the in-plane gradients of the order parameter phase $\nabla_{x,y}\theta_n$, which then, through the second Josephson relation $J_{n,n+1} = J_c \sin(\Delta\theta_{n,n+1})$, makes the c-axis tunneling dependent on the in-plane spatial coordinate. The equations of motion for the JPPs are then

$$\ddot{J}_1 + 2\gamma_{J_1}\dot{J}_1 + \omega_{J_1}^2(q_{x1}, q_{y1})J_1 = -aq^2 Q_{\text{drive}}(t)J_2,$$
$$\ddot{J}_2 + 2\gamma_{J_2}\dot{J}_2 + \omega_{J_2}^2(q_{x2}, q_{y2})J_2 = -aq^2 Q_{\text{drive}}(t)J_1,$$

where $\omega_{J_i}(q_{xi}, q_{yi})$ describe the in-plane equilibrium dispersion. These equations predict three-wave mixing between the apical oxygen phonons Q_{drive} and the upper
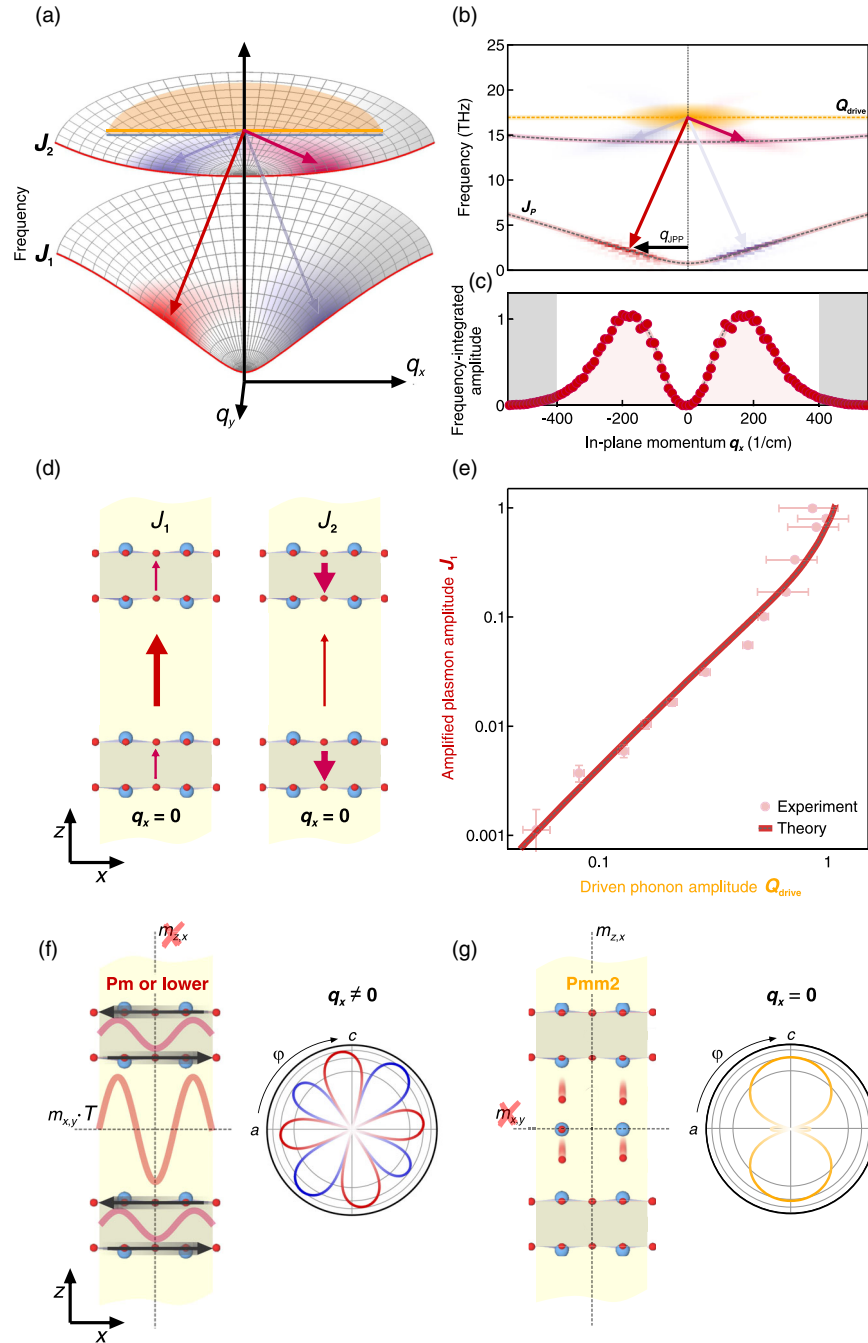
FIG. 5. (a) Dispersion of the interbilayer (J_1) and intrabilayer (J_2) JPP modes along the in-plane momenta q_x and q_y in YBa$_2$Cu$_3$O$_{6.5}$. The red lines are a cut through the $q_y = 0$ plane. The apical oxygen phonon mode at 17 THz (yellow) does not disperse along either direction. The three-wave scattering process is sketched as red and blue arrows and results from a numerical simulation in response to the resonant drive of the apical oxygen phonon at $q = 0$ are shaded in the same colors. The response vanishes along q_y, parallel to the light propagation direction. (b) Detailed insight into the simulation results along q_x for $q_y = 0$. The driven phonon with zero momentum excites a pair of JPPs, J_1 and J_2, with opposite wave vectors q_{JPP} and frequencies that add up to the phonon frequency. The two processes for mirrored momentum transfer are shown as red and blue arrows, respectively. (c) Amplitude of the JPPs obtained integrating along the vertical frequency axis of (b). The amplitude is zero for $q_x = 0$, and peaks at $q_x = \pm 200$ cm^{-1}. (d) Sketch of the two JPPs at $q = 0$, with the supercurrents oscillating in phase (J_1) or out of phase (J_2) for the low- and high-frequency mode, respectively. The thicknesses of the arrows indicate the supercurrent strengths within and between the bilayers. (e) Simulated excitation-strength dependence (dashed line) of the low-frequency 2.5-THz oscillations, together with the experimental data (dots) from Fig. 2(g). (f),(g) Sketch of the real-space symmetries of the finite-momentum amplified JPP (m or lower) and the driven apical oxygen vibration ($mm2$). The in-plane currents (black arrows) and the resulting finite-momentum JPP (red and magenta lines) break the x, z and y, z mirror planes. The optical B_{1u}-symmetry phonons break the x, y mirror plane only.

and lower JPPs, leading to the excitation of damped harmonic oscillations for J_1 and J_2 at finite momenta along the two-dimensional dispersion curves of Fig. 5(a), with a driving term $aq^2 Q_{\text{drive}}(t)J_{2,1}$. Note that the driving term depends on the momentum of the JPP as q^2, hence it vanishes for long wavelengths ($q = 0$) but naturally couples to supercurrents at finite in-plane wave vectors, as observed experimentally in the measurements of Fig. 4. The two equations predict further that the phonon excites pairs of JPPs with frequencies that satisfy $\omega_1 + \omega_2 = \omega_{\text{drive}}$, and opposite in plane momenta ($q_{x1} = -q_{x2}$ or $q_{y1} = -q_{y2}$).

A numerical solution of these equations of motion is displayed in the color-coded JPP dispersion of Figs. 5(a) and 5(b). There, the three-wave mixing process is shown to couple the driven phonon to JPPs at in-plane momenta $q_x \sim 200 \text{ cm}^{-1}$ [see Fig. 5(c)] where phase matching is fulfilled. The linear dependence of the driving terms on $J_{2,1}$ requires nonvanishing Josephson current amplitudes to seed this process. This is numerically accomplished by including stochastic variations of the supercurrents, equivalent to small phase fluctuations between the CuO_2 layers that will be transiently synchronized by the coupling to the optically excited phonon Q_{drive}. Note that the momentum at which excitation of J_1 and J_2 is expected matches very well the experimental findings reported in Fig. 4, despite it being obtained here from first principles and starting from the documented inductive response of $YBa_2Cu_3O_{6+x}$. Yet, the theory does not capture the experimentally observed asymmetry in peak amplitudes between the two scattering directions, which can most likely be attributed to the oblique experimental geometry. Since the midinfrared pump field and hence the driven phonons extend in the direction perpendicular to the optical surface only over a skin depth of $\sim 1.5 \mu$m, phase matching is inefficient along y. Hence, the excited pairs of high (intrabilayer) and low (interbilayer) frequency JPPs propagate along the optical surface like $J_1(\omega_1, +q_x)$ and $J_2(\omega_2, -q_x)$, or $J_1(\omega_1, -q_x)$ and $J_2(\omega_2, +q_x)$.

The theoretically predicted energy and momentum matching is consistent with the experimentally determined frequency resonance ($\omega_{\text{drive}} \sim 17$ THz, $\omega_1 \sim 2.5$ THz, $\omega_2 \sim 14.5$ THz), documented in the Supplemental Material [24], and is also consistent with the reported momentum-resolved measurements of Fig. 4. Furthermore, the calculated exponential amplification of the JPP, shown in Fig. 5(e), resembles the experimental results reported in Fig. 2.

Finally, the calculated real-space current patterns of these finite-momentum modes are sketched in Fig. 5(f) and compared to the real-space oscillations of the driven apical oxygen mode in Fig. 5(g). As explained by the theory, in-plane currents (drawn as black arrows) drive finite-momentum c-axis tunneling currents J_1 and J_2 (dashed lines), which break the two mirror planes perpendicular to

the CuO_2 layers ($m_{z,y}$ and $m_{z,x}$), in agreement with the SH polarimetry signal reported in Fig. 3.

In the following, we show that this theory naturally explains also the transient reflectivity edges reported in previous time-resolved terahertz probe experiments. The three-wave mixing excitation results in two counterpropagating JPPs with opposite momentum $\pm q_{\text{JPP}}$, which interfere to produce a standing wave pattern of the superconducting phase θ along the sample surface x direction [see Fig. 6(a)] as $\theta(x, t) = \theta_0 \cos(q_{\text{JPP}} \cdot x) \sin(\omega_{\text{JPP}} \cdot t)$. Through the Josephson equations, the dynamics of the phase $\theta(x, t)$ can be recast as a source of modulation of the in-plane superfluid density $\rho_s(x, t)$ at $q_x = 0$ as $\rho_s(x, t) = \rho_{s,0} \cos[\theta(x, t)]$, sketched in Fig. 6(b). For finite excursions of the condensate phase [$\theta(x, t) \ll \pi/2$], two salient features emerge at lowest-order expansion, that is, a spatial modulation of the superfluid density at $2q_{\text{JPP}}$ and a temporal modulation at $2\Omega(q_{\text{JPP}})$ at in-plane momentum $q_x = 0$:

$$\rho_s(x, t) \approx \rho_{s,0}\big(1 - \{\theta_0^2 + \theta_0^2 \cos(2q_{JP} \cdot x) \\ - \theta_0^2 \cos[2\Omega(q_{\text{JPP}}) \cdot t] \\ - \theta_0^2 \cos(2q_{\text{JPP}} \cdot x) \cos[2\Omega(q_{\text{JPP}}) \cdot t]\}/4\big).$$

Figure 6(c) illustrates this scenario. The two counterpropagating JPPs at $\pm q_{\text{JPP}}$ combine (red and blue arrows) to emit two photons [each frequency $\Omega(q_{\text{JPP}})$] at zero momentum. Naturally this process leads to parametric amplification of an optical terahertz probe at the same frequency.

From this model, following the Fresnel-Floquet approach described in Ref. [38], the transient terahertz reflectivity [13–16] can be computed both below and above T_c. Below T_c, as shown in Figs. 6(d) and 6(e), the theory predicts an additional plasma edge close to $\Omega(q_{\text{JPP}})$, notably above the equilibrium Josephson plasma edge of ~ 1 THz. This prediction compares well with the experimental reports, summarized in Figs. 6(h) and 6(i). In the temperature range $T_c < T < T^*$, the featureless equilibrium terahertz reflectivity is retrieved in these simulations by assuming the same interlayer Josephson coupling strength observed below T_c with a sizable increase in dephasing, as to make the JPP overdamped [38]. For a strong drive of the apical oxygen phonon, the plasma edge is predicted to reemerge close to $\Omega(q_{\text{JPP}})$ [see Figs. 6(f) and 6(g)], again blueshifted with respect to the below-T_c equilibrium resonance. At this frequency parametric driving compensates dissipation most efficiently and revives the features of the dissipationless state. In Figs. 6(j) and 6(k), we compare these calculations to experimental terahertz reflectivity data reported for a $YBa_2Cu_3O_{6.5}$ sample in Ref. [14] and find good agreement.

We conclude by noting that other trends in the data are supported by the line of argument laid out in this paper.
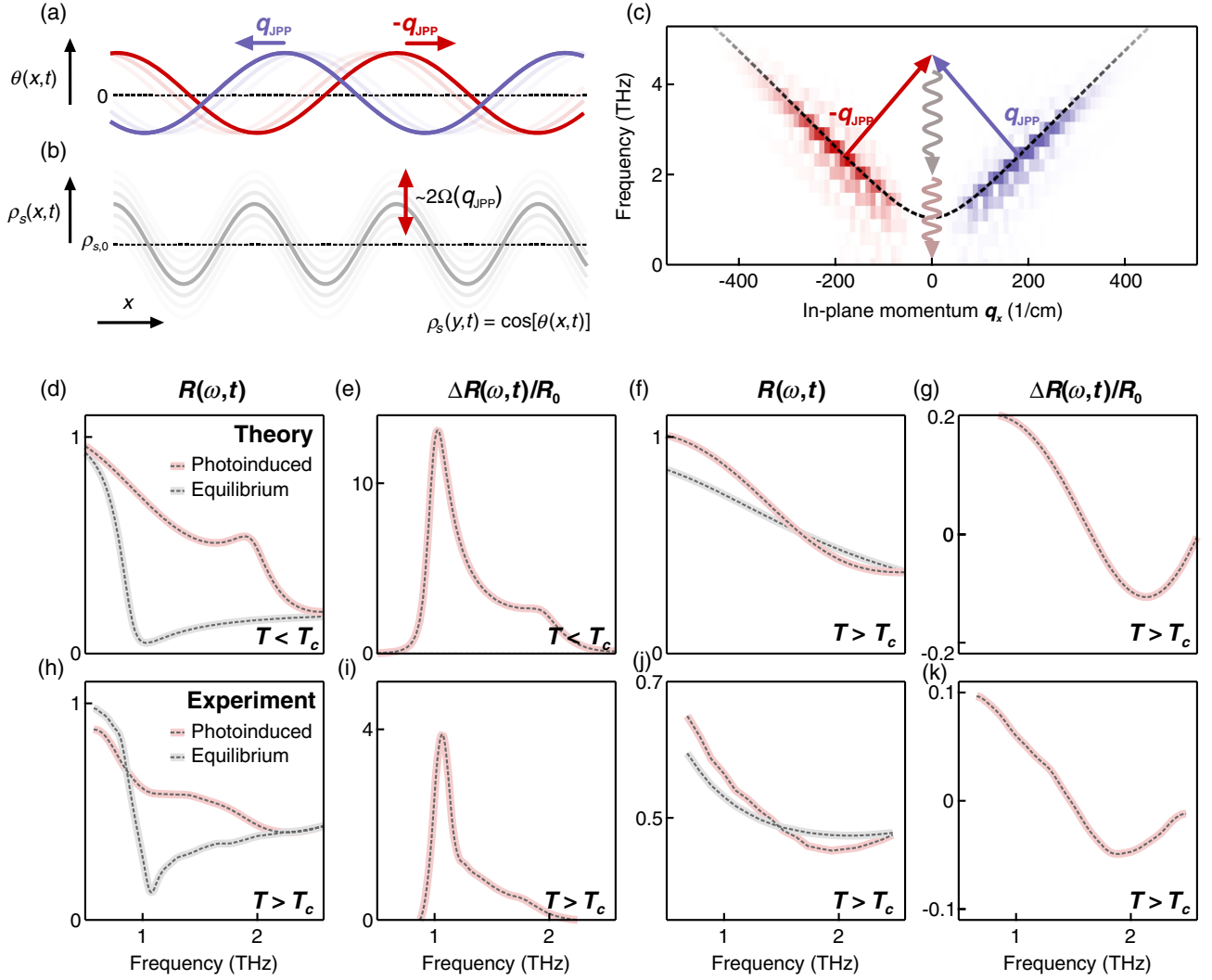
FIG. 6.   (a) Two counterpropagating JPPs with in-plane momentum q_{JPP} periodically modulate the superconducting order parameter $\theta(x, t)$ along the x axis. (b) Resulting spatial and temporal (shaded gray) modulation of the superfluid density $\rho_s(x, t)$ around its equilibrium value $\rho_{s,0}$. The zero-momentum temporal modulation proceeds at twice the Josephson plasma frequency $2\Omega(q_{JPP})$. (c) Frequency-momentum diagram of the parametric amplification that drives the terahertz emission. The two counterpropagating JPPs (red and blue shaded regions) add in energy and momentum to emit two $q_x = 0$ THz photons, each of frequency $\Omega(q_{JPP})$. (d),(e) Calculated photoinduced (red) and equilibrium (gray) terahertz reflectivity below T_c and the normalized reflectivity changes $\Delta R(\omega, t)/R_0$, respectively. The finite-momentum JPP induces a second plasma edge at a frequency close to $\Omega(q_{JPP})$ and overall enhancement of the reflectivity above the equilibrium plasma edge. (f),(g) Calculated photoinduced (red) and equilibrium (gray) terahertz reflectivity above T_c and the normalized reflectivity changes $\Delta R(\omega, t)/R_0$, respectively. Excitation of the apical oxygen vibration leads to the appearance of a plasma edge at a frequency close to $\Omega(q_{JPP})$, which is clearly visible in the normalized reflectivity changes $\Delta R(\omega, t)/R_0$. Panels (h)–(k) show the same features, observed experimentally in time-resolved terahertz reflectivity measurements after resonant excitation of apical oxygen oscillations (Ref. [14]).

The observed doping dependence for the induced reflectivity edge reported in Refs. [14,16] involves a response that extends to T^* for underdoped regions of the spectrum, but becomes negligible at higher doping, falling below T^*. The observed trends follow naturally from the requirement of a preexisting phase incoherent superconductivity *and* the need of resonant three-wave mixing discussed in Fig. 5. Because the three-wave mixing mechanism requires that $\omega_{drive} = \omega_{J_1} + \omega_{J_2}$, with the in-plane momentum chosen to

fulfill this condition along the dispersing branches of the JPPs, this effect is only possible for doping levels for which $\omega_{J_1,q=0} + \omega_{J_2,q=0} < \omega_{drive}$. This condition is fulfilled for $YBa_2Cu_3O_{6.48}$ and $YBa_2Cu_3O_{6.65}$, with $\omega_{J_1}^{6.48} = 2.5$ THz and $\omega_{J_1}^{6.65} = 2.8$ THz, but not for higher doping levels, where $\omega_{J_1} + \omega_{J_2} > \omega_{drive}$ at all momenta. Indeed, results in $YBa_2Cu_3O_{6.92}$ reported in Supplemental Material [24] confirm that no amplification of JPPs takes place at

these doping values, also in agreement with the lack of a light-induced reflectivity edge reported in Refs. [14,16], even for those doping values in which $T^* > T_c$.

While the present measurement is not comprehensively addressing the entire pseudogap region of the phase diagram, in the doping range where the parametric resonance between phonons and Josephson plasma polaritons can be fulfilled, our results can convincingly be explained if one assumes preexisting fluctuating superconductivity up to T^*, over correlation lengths of several microns [39]. In support of this hypothesis one should mention that although optical signatures of superconductivity at large correlation lengths vanish at T_c [40,41], momentum integrated probes, like the superconducting Nernst effect [42–46], measurements of electrical noise [47], and optical spectroscopy [48], provide evidence of residual coherence in the normal state, to be validated by more comprehensive methods such as high-resolution resonant Inelastic x-ray scattering [49,50] and electron energy loss probes [51]. More broadly, our experiments open up new perspectives of frequency resonant wave mixing as a new means to control cooperative phenomena in quantum materials.

---

[1] M. Först, C. Manzoni, S. Kaiser, Y. Tomioka, Y. Tokura, R. Merlin, and A. Cavalleri, *Nonlinear Phononics as an Ultrafast Route to Lattice Control*, Nat. Phys. **7**, 854 (2011).

[2] M. Kozina, M. Fechner, P. Marsik, T. van Driel, J. M. Glownia, C. Bernhard, M. Radovic, D. Zhu, S. Bonetti, U. Staub, and M. C. Hoffmann, *Terahertz-Driven Phonon Upconversion in* SrTiO$_3$, Nat. Phys. **15**, 387 (2019).

[3] M. Rini, R. Tobey, N. Dean, J. Itatani, Y. Tomioka, Y. Tokura, R. W. Schoenlein, and A. Cavalleri, *Control of the Electronic Phase of a Manganite by Mode-Selective Vibrational Excitation*, Nature (London) **449**, 72 (2007).

[4] A. D. Caviglia, R. Scherwitzl, P. Popovich, W. Hu, H. Bromberger, R. Singla, M. Mitrano, M. C. Hoffmann, S. Kaiser, P. Zubko, S. Gariglio, J.-M. Triscone, M. Först, and A. Cavalleri, *Ultrafast Strain Engineering in Complex Oxide Heterostructures*, Phys. Rev. Lett. **108**, 136801 (2012).

[5] S. Schlauderer, C. Lange, S. Baierl, T. Ebnet, C. P. Schmid, D. C. Valovcin, A. K. Zvezdin, A. V. Kimel, R. V. Mikhaylovskiy, and R. Huber, *Temporal and Spectral Fingerprints of Ultrafast All-Coherent Spin Switching*, Nature (London) **569**, 383 (2019).

[6] M. Först, A. D. Caviglia, R. Scherwitzl, R. Mankowsky, P. Zubko, V. Khanna, H. Bromberger, S. B. Wilkins, Y.-D. Chuang, W. S. Lee *et al.*, *Spatially Resolved Ultrafast Magnetic Dynamics Launched at a Complex-Oxide Hetero-Interface*, Nat. Mater. **14**, 883 (2015).

[7] M. Buzzi, D. Nicoletti, M. Fechner, N. Tancogne-Dejean, M. A. Sentef, A. Georges, T. Biesner, E. Uykur, M. Dressel, A. Henderson *et al.*, *Photomolecular High-Temperature Superconductivity*, Phys. Rev. X **10**, 031028 (2020).

[8] A. S. Disa, M. Fechner, T. F. Nova, B. Liu, M. Först, D. Prabhakaran, P. G. Radaelli, and A. Cavalleri, *Polarizing an Antiferromagnet by Optical Engineering of the Crystal Field*, Nat. Phys. **16**, 937 (2020).

[9] T. F. Nova, A. S. Disa, M. Fechner, and A. Cavalleri, *Metastable Ferroelectricity in Optically Strained* SrTiO$_3$, Science **364**, 1075 (2019).

[10] T. Kubacka, J. A. Johnson, M. C. Hoffmann, C. Vicario, S. de Jong, P. Beaud, S. Grübel, S.-W. Huang, L. Huber, L. Patthey *et al.*, *Large-Amplitude Spin Dynamics Driven by a THz Pulse in Resonance with an Electromagnon*, Science **343**, 1333 (2014).

[11] D. Afanasiev, J. R. Hortensius, B. A. Ivanov, A. Sasani, E. Bousquet, Y. M. Blanter, R. V. Mikhaylovskiy, A. V. Kimel, and A. D. Caviglia, *Ultrafast Control of Magnetic Interactions via Light-Driven Phonons*, Nat. Mater. **20**, 607 (2021).

[12] X. Li, T. Qiu, J. Zhang, E. Baldini, J. Lu, A. M. Rappe, and K. A. Nelson, *Terahertz Field–Induced Ferroelectricity in Quantum Paraelectric* SrTiO$_3$, Science **364**, 1079 (2019).

[13] W. Hu, S. Kaiser, D. Nicoletti, C. R. Hunt, I. Gierz, M. C. Hoffmann, M. L. Tacon, T. Loew, B. Keimer, and A. Cavalleri, *Optically Enhanced Coherent Transport in* YBa$_2$Cu$_3$O$_{6.5}$ *by Ultrafast Redistribution of Interlayer Coupling*, Nat. Mater. **13**, 705 (2014).

[14] S. Kaiser, C. R. Hunt, D. Nicoletti, W. Hu, I. Gierz, H. Y. Liu, M. Le Tacon, T. Loew, D. Haug, B. Keimer, and A. Cavalleri, *Optically Induced Coherent Transport Far above* T_c *in Underdoped* YBa$_2$Cu$_3$O$_{6+\delta}$, Phys. Rev. B **89**, 184516 (2014).

[15] B. Liu, M. Först, M. Fechner, D. Nicoletti, J. Porras, B. Keimer, and A. Cavalleri, *Two Pump Frequency Resonances for Light-Induced Superconductivity in* YBa$_2$Cu$_3$O$_{6.5}$, Phys. Rev. X **10**, 011053 (2020).

[16] C. R. Hunt, D. Nicoletti, S. Kaiser, D. Pröpper, T. Loew, J. Porras, B. Keimer, and A. Cavalleri, *Dynamical Decoherence of the Light Induced Inter Layer Coupling in* YBa$_2$Cu$_3$O$_{6+\delta}$, Phys. Rev. B **94**, 224303 (2016).

[17] M. Först, A. Frano, S. Kaiser, R. Mankowsky, C. R. Hunt, J. J. Turner, G. L. Dakovski, M. P. Minitti, J. Robinson, T. Loew, M. Le Tacon, B. Keimer, J. P. Hill, A. Cavalleri, and S. S. Dhesi, *Femtosecond X Rays Link Melting of Charge-Density Wave Correlations and Light-Enhanced Coherent Transport in* YBa$_2$Cu$_3$O$_{6.6}$, Phys. Rev. B **90**, 184514 (2014).

[18] R. Mankowsky, A. Subedi, M. Först, S. Mariager, M. Chollet, H. Lemke, J. S. Robinson, J. M. Glownia, M. P. Minitti, A. Frano, M. Fechner, N. A. Spaldin, T. Loew, B. Keimer, A. Georges, and A. Cavalleri, *Nonlinear Lattice Dynamics as a Basis for Enhanced Superconductivity in* YBa$_2$Cu$_3$O$_{6.5}$, Nature (London) **516**, 71 (2014).

[19] R. Mankowsky, M. Fechner, M. Först, A. von Hoegen, J. Porras, T. Loew, G. L. Dakovski, M. Seaberg, S. Möller, G. Coslovich, B. Keimer, S. S. Dhesi, and A. Cavalleri, *Optically-Induced Lattice Deformations, Electronic Structure Changes and Enhanced Superconductivity in* YBa$_2$Cu$_3$O$_{6.48}$, Struct. Dyn. **4**, 044007 (2017).

[20] A. Sell, A. Leitenstorfer, and R. Huber, *Phase-Locked Generation and Field-Resolved Detection of Widely Tunable Terahertz Pulses with Amplitudes Exceeding* 100 MV/cm, Opt. Lett. **33**, 2767 (2008).

[21] C. Manzoni, M. Först, H. Ehrke, and A. Cavalleri, *Single-Shot Detection and Direct Control of Carrier Phase Drift of Midinfrared Pulses*, Opt. Lett. **35**, 757 (2010).

[22] M. Fiebig, V. V. Pavlov, and R. V. Pisarev, *Second-Harmonic Generation as a Tool for Studying Electronic and Magnetic Structures of Crystals: Review*, J. Opt. Soc. Am. B **22**, 96 (2005).

[23] R. Mankowsky, M. Först, T. Loew, J. Porras, B. Keimer, and A. Cavalleri, *Coherent Modulation of the* $YBa_2Cu_3O_{6+x}$ *Atomic Structure by Displacive Stimulated Ionic Raman Scattering*, Phys. Rev. B **91**, 094308 (2015).

[24] See Supplemental Material at http://link.aps.org/supplemental/10.1103/PhysRevX.12.031008 for a discussion of the nonlinear phonon-phonon coupling and the theoretical description of the Josephson plasmon polariton. The Supplemental Material also contains additional data, such as the doping dependence of the JPP, the full temperature dependences of the JPP and the phonons, an excitation frequency dependence and a more detailed discussion of the excitation strength dependence of the JPP mode. A methods section is further included.

[25] M. Cardona, R. K. Chang, G. Güntherodt, M. B. Long, and H. Vogt, *Light Scattering in Solids II*, Topics in Applied Physics (Springer, Berlin, 1982).

[26] A. von Hoegen, R. Mankowsky, M. Fechner, M. Först, and A. Cavalleri, *Probing the Interatomic Potential of Solids with Strong-Field Nonlinear Phononics*, Nature (London) **555**, 79 (2018).

[27] L. Zhao, C. A. Belvin, R. Liang, D. A. Bonn, W. N. Hardy, N. P. Armitage, and D. Hsieh, *A Global Inversion-Symmetry-Broken Phase inside the Pseudogap Region of* $YBa_2Cu_3O_y$, Nat. Phys. **13**, 250 (2017).

[28] J. Schützmann, S. Tajima, S. Miyamoto, Y. Sato, and R. Hauff, *Doping and Temperature Dependence of c-Axis Optical Phonons in* $YBa_2Cu_3O_y$ *Single Crystals*, Phys. Rev. B **52**, 13665 (1995).

[29] D. Munzar, C. Bernhard, A. Golnik, J. Humlicek, and M. Cardona, *Anomalies of the Infrared-Active Phonons in Underdoped* $YBa_2Cu_3O_y$ *as Evidence for the Intra-Bilayer Josephson Effect*, Solid State Commun. **112**, 365 (1999).

[30] C. C. Homes, T. Timusk, D. A. Bonn, R. Liang, and W. N. Hardy, *Optical Properties along the c-Axis of* $YBa_2Cu_3O_{6+x}$, *for* $x = 0.50 \rightarrow 0.95$ *Evolution of the Pseudogap*, Physica (Amsterdam) **254C**, 265 (1995).

[31] M. Grüninger, D. van der Marel, A. A. Tsvetkov, and A. Erb, *Observation of Out-of-Phase Bilayer Plasmon in* $YBa_2Cu_3O_{7-\delta}$, Phys. Rev. Lett. **84**, 1575 (2000).

[32] C. C. Homes, T. Timusk, D. A. Bonn, R. Liang, and W. N. Hardy, *Optical Phonons Polarized along the c Axis of* $YBa_2Cu_3O_{6+x}$, *for* $x = 0.5 \rightarrow 0.95$, Can. J. Phys. **73**, 663 (1995).

[33] A. Shekhter, B. J. Ramshaw, R. Liang, W. N. Hardy, D. A. Bonn, F. F. Balakirev, R. D. McDonald, J. B. Betts, S. C. Riggs, and A. Migliori, *Bounding the Pseudogap with a Line of Phase Transitions in* $YBa_2Cu_3O_{6+\delta}$, Nature (London) **498**, 75 (2013).

[34] A. Dienst, E. Casandruc, D. Fausti, L. Zhang, M. Eckstein, M. Hoffmann, V. Khanna, N. Dean, M. Gensch, S. Winnerl, W. Seidel, S. Pyon, T. Takayama, H. Takagi, and A. Cavalleri, *Optical Excitation of Josephson Plasma Solitons in a Cuprate Superconductor*, Nat. Mater. **12**, 535 (2013).

[35] Y. Laplace and A. Cavalleri, *Josephson Plasmonics in Layered Superconductors*, Adv. Phys. X **1**, 387 (2016).

[36] D. van der Marel and A. A. Tsvetkov, *Transverse-Optical Josephson Plasmons: Equations of Motion*, Phys. Rev. B **64**, 024530 (2001).

[37] T. Koyama, *Josephson Plasma Resonances and Optical Properties in High-T_c Superconductors with Alternating Junction Parameters*, J. Phys. Soc. Jpn. **71**, 2986 (2002).

[38] M. H. Michael, A. von Hoegen, M. Fechner, M. Först, A. Cavalleri, and E. Demler, *Parametric Resonance of Josephson Plasma Waves: A Theory for Optically Amplified Interlayer Superconductivity in* $YBa_2Cu_3O_{6+x}$, Phys. Rev. B **102**, 174505 (2020).

[39] V. J. Emery and S. A. Kivelson, *Importance of Phase Fluctuations in Superconductors with Small Superfluid Density*, Nature (London) **374**, 434 (1995).

[40] J. Corson, R. Mallozzi, J. Orenstein, J. N. Eckstein, and I. Bozovic, *Vanishing of Phase Coherence in Underdoped* $Bi_2Sr_2CaCu_2O_{8+x}$, Nature (London) **398**, 221 (1999).

[41] L. S. Bilbro, R. Valdes Aguilar, G. Logvenov, O. Pelleg, I. Bozovic, and N. P. Armitage, *Temporal Correlations of Superconductivity above the Transition Temperature in* $La_{2-x}Sr_xCuO_4$ *Probed by Terahertz Spectroscopy*, Nat. Phys. **7**, 298 (2011).

[42] Z. A. Xu, P. Ong, Y. Wang, T. Kakeshita, and S. Uchida, *Vortex-like Excitations and the Onset of Superconducting Phase Fluctuation in Underdoped* $La_{2-x}Sr_xCuO_4$, Nature (London) **406**, 486 (2000).

[43] Y. Wang, Z. A. Xu, T. Kakeshita, S. Uchida, S. Ono, Y. Ando, and N. P. Ong, *Onset of the Vortexlike Nernst Signal above* T_c *in* $La_{2-x}Sr_xCuO_4$ *and* $Bi_2Sr_{2-y}La_yCuO_6$, Phys. Rev. B **64**, 224519 (2001).

[44] J. Chang, N. Doiron-Leyraud, F. Laliberté, R. Daou, D. LeBoeuf, B. J. Ramshaw, R. Liang, D. A. Bonn, W. N. Hardy, C. Proust, I. Sheikin, K. Behnia, and L. Taillefer, *Nernst Effect in the Cuprate Superconductor* $YBa_2Cu_3O_y$: *Broken Rotational and Translational Symmetries*, Phys. Rev. B **84**, 014507 (2011).

[45] O. Cyr-Choinière, R. Daou, F. Laliberte, C. Collignon, S. Badoux, D. LeBoeuf, J. Chang, B. J. Ramshaw, D. A. Bonn, W. N. Hardy, R. Liang, J.-Q. Yan, J.-G. Cheng, J.-S. Zhou, J. Goodenough, S. Pyon, T. Takayama, H. Takagi, N. Doiron-Leyraud, and L. Taillefer, *Pseudogap Temperature* T^* *of Cuprate Superconductors from the Nernst Effect*, Phys. Rev. B **97**, 064502 (2018).

[46] R. Daou, J. Chang, D. LeBoeuf, O. Cyr-Choinière, F. Laliberté, N. Doiron-Leyraud, B. J. Ramshaw, R. Liang, D. A. Bonn, W. N. Hardy, and L. Taillefer, *Broken Rotational Symmetry in the Pseudogap Phase of a High-T_c Superconductor*, Nature (London) **463**, 519 (2010).

[47] P. Zhou, L. Chen, Y. Liu, I. Sochnikov, A. T. Bollinger, M.-G. Han, Y. Zhu, X. He, I. Božović, and D. Natelson, *Electron Pairing in the Pseudogap State Revealed by Shot Noise in Copper Oxide Junctions*, Nature (London) **572**, 493 (2019).

[48] A. Dubroka, M. Rössle, K. W. Kim, V. K. Malik, D. Munzar, D. N. Basov, A. A. Schafgans, S. J. Moon, C. T. Lin, D. Haug, V. Hinkov, B. Keimer, T. Wolf, J. G. Storey, J. L. Tallon, and C. Bernhard, *Evidence of a Precursor*

Superconducting Phase at Temperatures as High as 180 K in $RBa_2Cu_3O_{7+x}$ *(R = Y, Gd, Eu) Superconducting Crystals from Infrared Spectroscopy*, Phys. Rev. Lett. **106,** 047006 (2011).

[49] W. S. Lee, I. M. Vishik, K. Tanaka, D. H. Lu, T. Sasagawa, N. Nagaosa, T. P. Devereaux, Z. Hussain, and Z.-X. Shen, *Abrupt Onset of a Second Energy Gap at the Superconducting Transition of Underdoped Bi2212*, Nature (London) **450,** 81 (2007).

[50] M. Hepting, L. Chaix, E. W. Huang, R. Fumagalli, Y. Y. Peng, B. Moritz, K. Kummer, N. B. Brookes, W. C. Lee, M. Hashimoto, T. Sarkar, J.-F. He, C. R. Rotundu, Y. S. Lee, R. L. Greene, L. Braicovich, G. Ghiringhelli, Z.-X. Shen, T. P. Devereaux, and W. S. Lee, *Three-Dimensional Collective Charge Excitations in Electron-Doped Copper Oxide Superconductors*, Nature (London) **563,** 374 (2018).

[51] M. Mitrano, A. A. Husain, S. Vig, A. Kogar, M. S. Rak, S. I. Rubeck, J. Schmalian, B. Uchoa, J. Schneeloch, R. Zhong, G. D. Gu, and P. Abbamonte, *Anomalous Density Fluctuations in a Strange Metal*, Proc. Natl. Acad. Sci. U.S.A. **115,** 5392 (2018).